












Cite this: *J. Mater. Chem. A*, 2023, 11, 16659

Probing the redox capacity of Pt–CeO₂ model catalyst for low-temperature CO oxidation†

Alexander Simanenکو, ^a Maximilian Kastenmeier, ^a Lesia Piliai, ^b Yuliia Kosto, ^{‡b} Tomáš Skála, ^b Nataliya Tsud, ^b Sascha Mehl, ^c Mykhailo Vorokhta, ^b Iva Matolínová, ^b Yaroslava Lykhach ^{*a} and Jörg Libuda ^a

The redox capacity of Pt–CeO₂ catalysts for low-temperature CO oxidation has been investigated by means of near-ambient pressure X-ray photoelectron spectroscopy, synchrotron radiation photoelectron spectroscopy, and resonant photoemission spectroscopy. The well-defined model Pt–CeO₂ systems containing specific Pt species which differ with respect to the oxidation state, chemical environment, and nuclearity, including atomically dispersed Pt²⁺ and Pt⁴⁺ species, metallic Pt⁰ nanoparticles, ultra-small Pt* aggregates, and PtO_x clusters were prepared by physical vapor co-deposition of Pt and Ce metals in an oxygen atmosphere onto a CeO₂(111) buffer layer on Ru(0001) and subsequent annealing under reducing or oxidizing conditions. The oxidation states of Pt species and Ce cations were monitored upon CO exposure as a function of temperature. We found that metallic Pt⁰ nanoparticles, ultra-small Pt*/PtO_x clusters, and Pt⁴⁺ species serve as CO adsorption sites at low temperature. Exclusively, the redox capacity for the low-temperature CO oxidation (below the room temperature) was observed only for the Pt–CeO₂ catalyst containing metallic Pt⁰ nanoparticles. The corresponding redox pathway is associated with CO spillover and the formation of bidentate carbonate species. Above 400 K, the redox interaction of CO with model Pt–CeO₂ catalysts involves the Mars–van Krevelen mechanism regardless of the nature of the Pt species.

Received 26th April 2023
Accepted 1st July 2023

DOI: 10.1039/d3ta02507a

rsc.li/materials-a

Introduction

Strict regulations of emission standards¹ stimulated the development of CO oxidation catalysts operating under low-temperature conditions.^{2–5} Besides emission control, low-temperature oxidation (LTO) of CO attracts great interest due to its high relevance for many industrial processes, particularly in the petrochemical industry, for the synthesis of pure gases, and for clean hydrogen production.^{2–7} Also, from a fundamental point of view, CO oxidation is of great interest as it is a prototype reaction for determining the activity of oxidation catalysts.⁸ Multicomponent systems which contain platinum-group metals as the active phase and reducible oxides as supports show high

activity for LTO of CO.^{9–14} In these materials, metallic Pt is found in the form of nanoparticles (Pt⁰ NPs) or clusters, oxidized NPs or clusters, and atomically dispersed species. It is known that the Pt undergoes dynamic structural transformations between these forms depending on the reaction conditions.^{11,14,15}

In recent studies by Boronin *et al.*,^{16–18} Pt-doped cerium oxide (Pt–CeO₂) showed exceptionally high catalytic activity for CO oxidation at temperatures below 273 K. The authors proposed an associative (concerted) mechanism that involves the reaction of weakly adsorbed O₂ and CO molecules at PtO_x clusters on Pt-doped CeO₂. The latter contained atomically dispersed Pt²⁺ and Pt⁴⁺ species.¹⁶ It was discussed that the Pt²⁺ and Pt⁴⁺ species do not contribute directly to the LTO of CO but are essential for the formation of ultra-small PtO_x clusters. Earlier, we investigated the transformation of Pt species in model Pt–CeO₂ catalysts as a function of Pt loading and thickness.^{6,19,20} We found that annealing triggers the segregation of ionic Pt species to the surface of the Pt–CeO₂ film. During this process, ionic Pt species can be trapped at the surface in the form of Pt²⁺ species anchored in a square planar oxygen coordination environment at {100} nano-pocket sites. If the number of ionic Pt species exceeds the number of available {100} nano-pocket sites, a fraction of ionic Pt species undergoes reduction and sintering yielding ultra-small Pt* aggregates and Pt⁰ NPs. This process is

^aInterface Research and Catalysis, ECRC, Friedrich-Alexander-Universität Erlangen-Nürnberg, Egerlandstraße 3, 91058 Erlangen, Germany. E-mail: yaroslava.lykhach@fau.de

^bCharles University, Faculty of Mathematics and Physics, Department of Surface and Plasma Science, V Holešovičkách 2, Prague, 18000, Czech Republic

^cElettra-Sincrotrone Trieste SCpA, Strada Statale 14, km 163.5, Basovizza-Trieste, 34149, Italy

† Electronic supplementary information (ESI) available. See DOI: <https://doi.org/10.1039/d3ta02507a>

‡ Present address: Applied Physics and Semiconductor Spectroscopy, Brandenburg University of Technology Cottbus-Senftenberg, Konrad-Zuse-Straße 1, 03046 Cottbus, Germany.

particularly favorable upon annealing in reducing gas atmosphere, *e.g.*, in CO, CH₃OH, *etc.*^{7,21,22} The density of the Pt* aggregates and the Pt⁰ NPs depends strongly on the Pt loading and the degree of reduction of the CeO₂ support.

Based on this detailed understanding of the electronic structure of the model Pt–CeO₂ catalyst and its structural dynamics, we are now able to probe the CO interaction with specific Pt species and to obtain insight into the mechanism of low-temperature CO oxidation. In the present paper, we investigate the redox capacity of the Pt–CeO₂ catalysts containing different forms of platinum species, including Pt⁰ NPs, ultra-small Pt* aggregates and PtO_x clusters, and atomically dispersed Pt²⁺ and Pt⁴⁺ species. We monitor the oxidation states of platinum and ceria using near ambient pressure X-ray photoelectron spectroscopy (NAP-XPS), synchrotron radiation photoelectron spectroscopy (SRPES), and resonant photoemission spectroscopy (RPES) methods. We found that in the low-temperature region below 400 K, the Pt–CeO₂ catalysts show redox activity exclusively in the presence of Pt⁰ NPs. The changes in the oxidation state of the Pt–CeO₂ catalysts containing oxidized Pt species are the most prominent above 400 K and are related to a Mars–van Krevelen mechanism channel involving the CeO₂ support.

Experimental

Near ambient pressure X-ray photoelectron spectroscopy (NAP-XPS)

NAP-XPS was performed at Charles University in Prague, Czech Republic. The NAP-XPS setup (Specs GmbH, Germany) was equipped with a monochromatized Al K α (1486.6 eV) X-ray source, a multichannel electron energy analyzer (Phoibos 150) coupled with a differentially pumped electrostatic prelens system, a flood gun, a high-resolution CCD camera, and two ports fitted with gate valves separating the NAP chamber and vertical ultra-high vacuum (UHV) manipulators, respectively. The basic setup included a sputter gun (Ar⁺), low energy electron diffraction (LEED) optics, a gas dosing system, and two electron beam evaporators for the deposition of Ce and Pt metals. The NAP cell was installed on a manipulator inside the XPS analysis chamber. During the measurement, the NAP cell was docked at the entrance aperture of the analyzer. The base pressure in the analysis chamber was 5×10^{-10} mbar. The working pressure in the NAP cell was 1 mbar. The gases were dosed without additional purification. The sample was heated by electron bombardment at the back of the sample holder and at the back of the sample stage in thermal contact with the sample holder while mounted on the UHV and NAP manipulators, respectively. The temperature was monitored by a K-type thermocouple spot-welded to the side of the sample.

The model Pt–CeO₂/CeO₂(111) catalyst was prepared on a Ru(0001) single crystal (MaTecK, 99.99%). First, the Ru(0001) single crystal was cleaned by several cycles of Ar⁺ sputtering (300 K, 40 min) with consecutive flash annealing in UHV (750 K) until no traces of contaminants were found in the photoelectron spectra. Subsequently, a CeO₂(111) buffer layer was grown by physical vapor deposition (PVD) of Ce

metal (Goodfellow, 99.99%) onto the Ru(0001) surface in an oxygen atmosphere (2×10^{-7} mbar, Linde, 99.999%) at 523 K for 40 minutes, followed by flash annealing in oxygen (2×10^{-7} mbar) at 700 K. The corresponding procedure was based on earlier studies of the growth, structure, and crystallinity of the CeO₂(111) films prepared on Ru(0001).^{23–27} The preparation method yielded a continuous, stoichiometric CeO₂(111) film with a thickness of 2.5 nm as determined from the attenuation of the Ru 3d core level intensity. The structure, surface, orientation, and continuity of the CeO₂(111) film were verified by LEED (see ESI, Section S1†).

In the next step, Pt metal (Goodfellow, 99.99%) was co-deposited with Ce by PVD in 5×10^{-7} mbar of O₂ at 300 K with a deposition rate ratio of Pt/CeO₂ = 1/7 onto the CeO₂(111) buffer layer in a single deposition step. Note, that the purpose of the buffer layer was to prevent direct interaction between Pt and Ru(0001). The nominal thickness of the Pt–CeO₂ film was 1.0 nm. The prepared 12% Pt–CeO₂/CeO₂(111) sample was inserted into the NAP cell and annealed at different temperatures with 50 K step in a range from 300 to 550 K, first in 1 mbar of O₂ and then, subsequently, in UHV.

The Pt 4f, Ru 3d, C 1s, O 1s, and Ce 3d core level spectra were acquired at constant pass energy and emission angle of the photoelectrons of 0° with respect to the sample normal. The instrumental resolution of the NAP-XPS system was determined from the full width at half-maximum (FWHM) of the Ag 3d core level spectrum of 0.8 eV obtained from the Ag film at pass energy of 20 eV.

The data were processed, and spectra were fitted using the KolXPd fitting software.²⁸ All spectral components were fitted by a Voigt function after subtraction of the Shirley background. Pt 4f core level spectra were fitted with a fixed branching ratio of 1.33 and a spin–orbit splitting of 3.3 eV. All series of spectra are presented after normalization of the total peak areas to unity.

Synchrotron radiation photoelectron spectroscopy (SRPES) and resonant photoemission spectroscopy (RPES)

SRPES and RPES experiments were performed at the Material Science Beamline (MSB) at the Elettra synchrotron light facility in Trieste, Italy. The MSB was equipped with a bending magnet source and provides synchrotron light in the energy range of 22–1000 eV. The UHV end-station (base pressure 2×10^{-10} mbar) was equipped with a delay line electron energy analyzer (Specs Phoibos 150), a dual Mg/Al X-ray source, a rear-view LEED optics, a sputter gun (Ar⁺), and a gas inlet system. Additionally, two electron-beam evaporators for the deposition of Ce and Pt metals were installed. The sample temperature was controlled by a DC power supply passing a current through Ta wires holding the sample. The temperature was monitored by a K-type thermocouple spot-welded to the side of the sample.

Two samples containing 12% of Pt in the co-deposited Pt–CeO₂ oxide film with a nominal thickness of 1.7 nm, one sample of 0.4 nm 12% Pt–CeO₂, and one 0.4 nm 8% Pt–CeO₂ were prepared on Ru(0001) following the procedure described in the NAP-XPS section with minor alterations. The Ru(0001) single crystal (MaTecK, 99.99%) was cleaned by Ar⁺ sputtering (300 K,

75 min), followed by annealing in UHV (1000 K, 5 min) until no traces of contaminants were found in the photoelectron spectra. Then an epitaxial buffer CeO₂(111) film was deposited onto the Ru(0001) surface by PVD of Ce metal (Goodfellow, 99.99%) in an oxygen atmosphere (5×10^{-7} mbar, Linde, 99.999%) at 700 K for 60 min followed by annealing in oxygen (5×10^{-7} mbar) at 800 K for 5 min, and then annealed in UHV at 700 K for 3 min. The preparation method yielded a continuous, stoichiometric CeO₂(111) film with a thickness of 1.5–2.0 nm, as determined from the attenuation of the Ru 3d core level intensity. LEED observations on the prepared buffer layers confirmed epitaxial growth of CeO₂(111).

The mixed Pt–CeO₂ films were prepared using simultaneous PVD of Ce and Pt (Goodfellow, 99.99%) metals in an oxygen atmosphere (5×10^{-7} mbar) onto the CeO₂(111)/Ru(0001) at 100 K. The Pt concentration of 8% and 12% in the volume of the mixed layers was achieved by using Pt/CeO₂ deposition rate ratios of 1/12 and 1/7, respectively. The deposition rate ratios were determined from the ratios of the nominal thickness of Pt to CeO₂ deposited separately for the same period.

The nominal thickness of 0.4 and 1.7 nm of the Pt–CeO₂ oxide film was achieved by regulating the time of the co-deposition of Ce and Pt metals to 20 and 90 min, respectively. In the next step, the as-prepared samples were treated by annealing at different temperatures in UHV, in 10^{-6} mbar O₂ *in situ*, or in 1.6 mbar O₂ in the preparation chamber with a base pressure of 5×10^{-7} mbar.

During the experiment, the samples were exposed to 1×10^{-6} mbar of CO (Linde, 99.98%) at different temperatures with 25 K steps in a range from 100 to 400 K and with 50 K steps in a range from 400 to 700 K for 3 min in each step. After each exposure, the gas inlet valve was closed, then the annealing was switched off and the sample was cooled down in UHV. Afterwards, the valence band of Pt–CeO₂ and the core level spectra of Pt 4f, Ru 3d, C 1s, and O 1s were measured.

Core level spectra were acquired with photon energies of 180 (Pt 4f), 380 (Ru 3d, C 1s), and 650 eV (O 1s). Additionally, Al K α radiation (1486.6 eV) was used to measure Ce 3d core levels. The binding energies in the spectra were calibrated with respect to the Fermi level. All spectra were acquired at constant pass energy and emission angle of the photoelectrons of 0° or 20° with respect to the sample normal while using synchrotron radiation or the X-ray source, respectively.

Valence band spectra were acquired at three different photon energies of 115.0, 121.4, and 124.8 eV. Analysis of the spectra obtained with these photon energies forms the basis of RPES on ceria-based materials.^{19,20,29–32} Briefly, RPES is based on measuring the valence band photoemission spectra at photon energies corresponding to the 4d \rightarrow 4f resonance in Ce³⁺ and Ce⁴⁺ ions. The Ce³⁺ resonance at a photon energy of 121.4 eV is caused by a super Coster–Kronig decay involving electron emission from Ce 4f states located at about 1.4 eV. The Ce⁴⁺ resonance at a photon energy of 124.8 eV involves the emission of O 2p electrons (hybridized with Ce states) from the valence band around 4.0 eV. The valence band spectrum obtained with a photon energy of 115 eV corresponds to the ‘off-resonance’ condition. The resonant enhancements for Ce³⁺ and Ce⁴⁺,

denoted as D(Ce³⁺) and D(Ce⁴⁺), respectively, are quantified by calculating the intensity difference between the corresponding features on- and off-resonance. The ratio between the corresponding resonant intensities, D(Ce³⁺)/D(Ce⁴⁺), denoted as a resonant enhancement ratio (RER), is a direct measure of the degree of reduction of ceria and can be used to quantify the relative content of Ce³⁺ ions in the films.^{19,20,30–32} In particular, the RER scales with the Ce³⁺/Ce⁴⁺ concentration ratio by a factor of 5.5.^{19,20,32}

The values of the total spectral resolution were 200 (photon energy 115–180 eV), 360 (380 eV), 650 meV (650 eV), and 1 eV (Al K α). To process the obtained SRPES data and analyze the spectra, the KolXPDS fitting software was used.²⁸ The spectral components in the Pt 4f core level spectra were fitted the same way as in the NAP-XPS method. All series of spectra are presented after normalization of the total peak areas to unity.

Results and discussion

The nature of Pt species under oxidizing conditions

To investigate the nature of Pt species formed under strongly oxidizing conditions in the Pt–CeO₂ model catalyst, we applied the method of NAP-XPS. The experiment involved annealing of the as-prepared 12% Pt–CeO₂ model catalyst in 1 mbar O₂ between 300 and 550 K. The evolution of Pt 4f spectra is shown in Fig. 1a. Before annealing, the Pt 4f core level spectrum obtained from the as-prepared Pt–CeO₂ model catalyst (top spectrum in Fig. 1a) comprises of two doublet peaks at 72.8 eV (Pt 4f_{7/2}) and 71.7 eV (Pt 4f_{5/2}) associated with Pt²⁺ species^{6,7,19,20,22} and Pt⁰ NPs,^{7,19,20,22,32} respectively. Typically, the most stable Pt²⁺ species anchored in square planar oxygen coordination at {100} nano-pocket sites of the CeO₂ give rise to a spectral contribution at 73.0 eV.^{6,7,19,20,22,33,34} However, the slightly lower binding energy of the Pt²⁺ contribution in the Pt–CeO₂ model catalyst prepared at 300 K suggests that a fraction of Pt²⁺ species exist in different chemical environments. The less stable Pt²⁺ species and Pt⁰ NPs result from a shortage of {100} nano-pocket sites on Pt–CeO₂ model catalysts.^{6,20}}}

Upon exposure of the as-prepared Pt–CeO₂ model catalyst to oxygen, the binding energy of Pt²⁺ contribution gradually shifted to 72.3 eV at 550 K. The Pt⁰ contribution decreased until it completely vanished at 350 K. In parallel, a new peak emerged at 74.3 eV, which corresponds to highly oxidized Pt⁴⁺ species.^{35–37} During annealing in the oxygen atmosphere, the binding energy of the Pt⁴⁺ contribution also shifts towards lower binding energies (73.8 eV).

In the next step, we cooled the sample in 1 mbar O₂ from 550 to 300 K and evacuated the NAP cell. The corresponding Pt 4f core level spectrum is shown in Fig. 1b. Evacuation of the NAP cell resulted in a slight increase of the Pt²⁺ contribution at the expense of Pt⁴⁺, while the binding energies of the Pt²⁺ and Pt⁴⁺ components shifted to 72.6 and 74.2 eV, respectively. The shifts of the Pt 4f contributions correlate with the shifts of O 1s contributions (data not shown) and result from band bending in the oxide film in the presence of O₂ gas under NAP conditions.³⁸

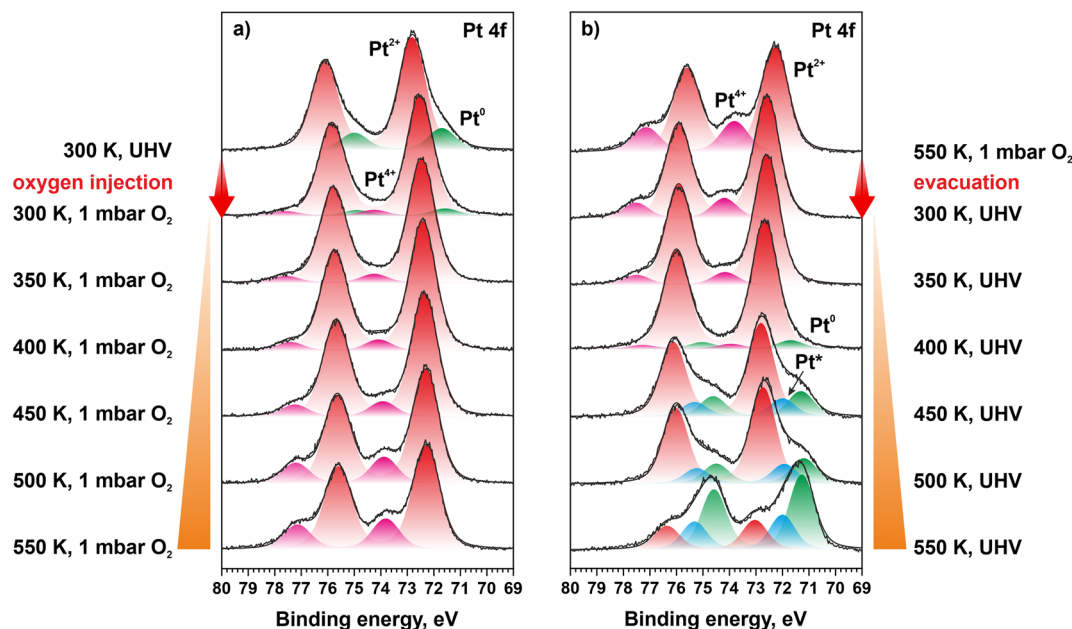


Fig. 1 Pt 4f core level spectra obtained from 1.0 nm 12% Pt–CeO₂ model catalyst by means of NAP-XPS as a function of temperature in 1 mbar O₂ (a) and subsequent annealing in UHV (b). The Pt 4f spectra were acquired with Al K α radiation (1486.6 eV).

The following annealing in UHV resulted in the emergence of Pt⁰ and Pt* components at 71.7 (Pt 4f_{7/2}) and 72.0 eV (Pt 4f_{5/2}) at 400 and 450 K, respectively, and the disappearance of the Pt⁴⁺ species at 450 K. Above 400 K, the Pt* and Pt⁰ contributions continue to grow at the expense of Pt²⁺. The decrease of the Pt²⁺ contribution is accompanied by a shift to 73.0 eV. The observed behavior suggests that the reduction of Pt⁴⁺ species yields Pt²⁺ species, while the reduction of Pt²⁺ species yields Pt⁰ NPs and Pt* aggregates.

The overall thermal stability and transitions of the Pt species are in good agreement with the behavior of radio frequency (RF)-sputtered highly oxidized platinum NPs as reported by Svintitskiy *et al.*³⁷

Overview of Pt species in Pt–CeO₂ model catalysts

The redox properties of the Pt–CeO₂ model catalyst were investigated as a function of the nature of the Pt species by means of SRPES and RPES. The morphology and composition of the samples is schematically illustrated in Fig. 2.

Three types of as-prepared Pt–CeO₂ model catalysts, denoted as samples 1.0, 2.0, and 3.0, were prepared at 100 K, which differ with respect to the thickness and Pt loading (see Fig. 2, left column). The sample with a nominal thickness of the Pt–CeO₂ film of 1.7 nm (sample 1.0) allows us to reproduce the effect of Pt segregation observed in the real catalysts under operation conditions.^{16,39} In contrast, this effect is minimized in the samples with a nominal thickness of the Pt–CeO₂ film of 0.4 nm (samples 2.0 and 3.0). The purpose of samples 2.0 and 3.0 with different Pt loadings was to address the effect of the shortage of {100} nano-pocket sites on the redox properties of the Pt–CeO₂ model catalysts. Typically, the density of {100} nano-pocket sites depends on the degree of

nanostructuring of the Pt–CeO₂ catalyst, which is a function of preparation temperature.²¹ Thus, the Pt–CeO₂ catalyst prepared at 100 K has higher amount of {100} nano-pocket sites as compared to the one prepared at 300 K. Annealing of the Pt–CeO₂ catalyst reduces the amount of {100} nano-pocket sites due to temperature-driven coarsening of the films.²¹ Shortage of {100} nano-pocket sites results in the formation of less stable Pt species prone to reduction or oxidation depending on the experimental conditions.

Based on samples 1.0, 2.0, and 3.0, we prepared three sets of model Pt–CeO₂ catalysts containing Pt species typically found under reducing and oxidizing conditions. For this purpose, we annealed the as-prepared samples 1.0–3.0 in UHV and at two different oxygen pressures, *i.e.*, 1.6 mbar and 1 × 10^{−6} mbar O₂. The Pt 4f spectra obtained before and after the treatments of the as-prepared samples 1.0 to 3.0 specified in Fig. 2 are shown in Fig. 3a and b.

In all cases, the as-prepared samples predominantly contained Pt²⁺ (72.5–72.9 eV) species accompanied by a minor amount of Pt⁴⁺ (73.9–74.3 eV) species (Fig. 3a). Note that the Pt⁴⁺ species in the as-prepared Pt–CeO₂ films deposited at 100 K are located in the bulk.¹⁹ Upon annealing, these species segregate to the surface and are stabilized in the form of Pt²⁺ ions in {100} nano-pocket sites if available.²¹ The annealing of thick Pt–CeO₂ films (sample 1.0) under reducing (700 K in UHV) and strongly oxidizing (550 K in 1.6 mbar O₂) conditions yielded samples 1.1 and 1.2. The corresponding treatments triggered the Pt segregation leading to Pt enrichment at the surface (both for samples 1.1 and 1.2).¹⁹ Note that based on our earlier study,¹⁹ we exclude diffusion and accumulation of Pt at the CeO₂(111)/Ru(0001) interface. To quantify the enrichment of Pt at the surface, we estimated the density of Pt

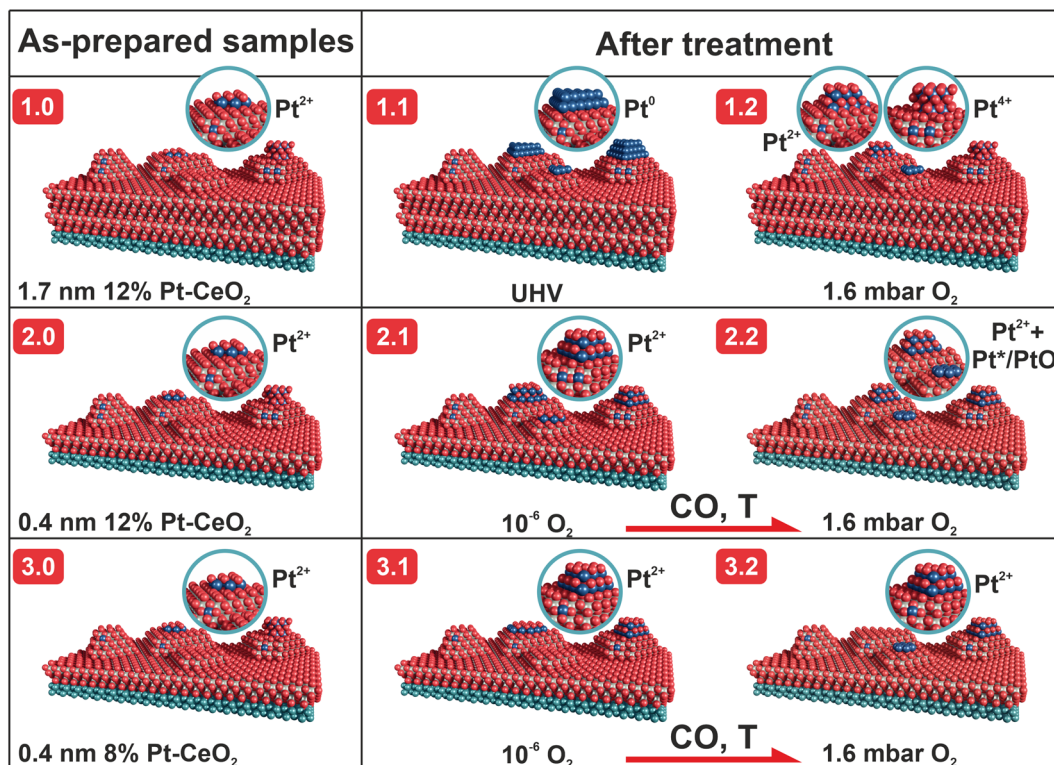


Fig. 2 Schematic representation of the morphology and composition of the Pt–CeO₂ model catalysts before and after the treatment under different experimental conditions. The most abundant Pt species are shown in the insets.

atoms in the co-deposited films for samples 1.0 and 2.0 (12% Pt loading, nominal thicknesses of 1.7 nm and 0.4 nm, respectively). Based on the thickness ratio, we found that the concentration of Pt at the surface of sample 1.0 is higher than on sample 2.0 by a factor of 4.25. Upon annealing in UHV (sample 1.1), segregation of Pt and partial reduction of Pt²⁺ species yield mainly Pt⁰ NPs accompanied by a small number

of Pt* aggregates and Pt²⁺ species in {100} nano-pocket sites.¹⁹ The corresponding contributions appear in the spectra at 71.0 eV (Pt⁰), 72.0 eV (Pt*), and 72.8 eV (Pt²⁺) (see Fig. 3b). In contrast, the main species formed under strongly oxidizing conditions upon annealing in 1.6 mbar O₂ (sample 1.2) are Pt²⁺ species in {100} nano-pockets and other less favorable sites accompanied by a small amount of Pt⁴⁺ species and only

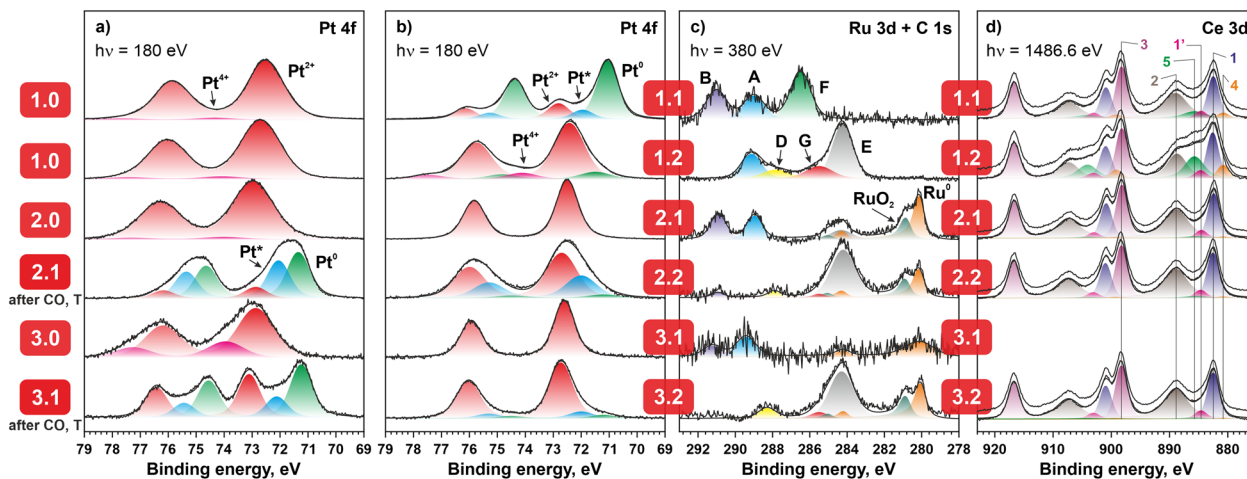


Fig. 3 Pt 4f (a and b), Ru 3d and C 1s (c), and Ce 3d (d) core level spectra obtained from the Pt–CeO₂ model catalysts before (a) and after (b–d) the treatments specified in Fig. 2; the spectra in (c and d) were obtained before (lower spectra in (d)) and after CO exposure at 100 K ((c), upper spectra in (d)). The Pt 4f and Ru 3d + C 1s spectra were acquired with photon energies of 180 and 380 eV, respectively. The Ce 3d spectra were acquired with Al K α radiation ($h\nu = 1486.6$ eV).

traces of Pt⁰ NPs. The corresponding contributions were observed at 72.4 eV (Pt²⁺), 74.1 eV (Pt⁴⁺), and 71.5 eV (Pt⁰) (see Fig. 3b).

The nature of the Pt species formed under mild oxidizing conditions was investigated on model Pt–CeO₂ catalysts with a nominal thickness of 0.4 nm prepared with two different Pt loadings, *i.e.*, 12% and 8% (samples 2.0 and 3.0). Both samples were annealed at 700 K in 10^{−6} mbar of O₂. The resulting samples are denoted as 2.1 and 3.1, respectively. The corresponding treatment yielded predominantly Pt²⁺ species in {100} nano-pockets accompanied by a fraction of less favorable sites. Based on the binding energies, we propose that the fraction of stable Pt²⁺ species in the {100} nano-pockets is higher on sample 3.1 than on sample 2.1.

Finally, we annealed samples 2.1 and 3.1 in CO at 700 K and, subsequently, at 550 K in 1.6 mbar of O₂ (obtaining samples 2.2 and 3.2, respectively). This procedure resulted in formation of Pt²⁺ species in {100} nano-pockets accompanied by a fraction of Pt in less favorable sites. Since the initial samples 2.1 and 3.1 contain large amounts of Pt⁰ and Pt*, it is likely that after the treatment under strongly oxidizing conditions, these species are converted to less stable Pt²⁺ species and PtO_x clusters. Still, both samples 2.2 and 3.2 contain trace amounts of Pt* aggregates and Pt⁰ NPs. Note that the spectral features of the Pt* contribution (72.0 eV) overlap with those of the PtO compound (72.3 eV).³⁶ As a result, the two contributions cannot be resolved spectroscopically. We assume that the amount of less stable Pt²⁺ species and PtO_x clusters is higher in the samples 2.2 and 3.2 as compared to 2.1 and 3.1, respectively.

Based on the comparison of the Pt species identified in the Pt 4f spectra in Fig. 3b, we conclude that the Pt⁴⁺ species and Pt⁰ NPs on samples 1.1 and 1.2 are formed exclusively by Pt segregation to the surface of the Pt–CeO₂ model catalysts.

Additionally, we probed the CO adsorption sites on all samples at 100 K. The Ru 3d + C 1s spectra are compared in Fig. 3c. The nature of the CO-derived species and the corresponding chemical environment of the adsorption sites can be assigned based on our earlier study.²¹ We identify the peaks in the Ru 3d + C 1s region as follows: peak A (289.0–289.4 eV) and peak B (290.9–291.2 eV) are tridentate and bidentate carbonate species on the nanostructured stoichiometric CeO₂ film, respectively. Peak E (284.2–284.3 eV) represents adventitious carbon on the ceria surface formed during the treatment of the samples in the preparation chamber (see Experimental section).²¹ The origin of the adventitious carbon is not related to the interaction of CO with the samples. Peak F (286.5 eV) indicates CO adsorption on Pt⁰ NPs in on-top configuration. In addition to these peaks, we observed a component G (285.5 eV) in samples 1.2, 2.2, and 3.2. The binding energy of this component is lower than the value typically observed for CO in the bridge-bonded configuration (286.1 eV) on flat⁴⁰ and rough⁴¹ Pt(111) surfaces. The species characterized by a low binding energy (285.6 eV) has been earlier assigned to CO adsorbed at the Pt-ceria interface.⁴² Considering the low amount of metallic Pt in treated samples 1.2, 2.2, and 3.2, we assign the peak G to CO adsorbed at the low-coordinated Pt sites in direct contact with CeO₂. Surprisingly, we resolved ruthenium oxide (280.8 eV)

along with metallic ruthenium (280.1 eV) in the Pt–CeO₂ samples with a thickness of 0.4 nm upon treatment in oxygen and CO. The appearance of RuO₂ indicates the presence of exposed spots of Ru(0001) single crystal on the surface and their oxidation upon the oxygen treatment.

The most important observation is the occurrence of the peak D (287.8–288.3 eV) associated with CO adsorption at cationic sites. Earlier, we assigned peak D to CO adsorbed at Ce³⁺ cations. On samples prepared under strongly oxidizing conditions, such cationic sites are Pt⁴⁺ sites (sample 1.2) and Ru⁴⁺ sites (samples 2.2 and 3.2). Therefore, we note that Pt⁰ NPs and Pt⁴⁺/Ru⁴⁺ cations serve as adsorption sites for CO.

The Ce 3d spectra obtained from the treated samples before and after the first exposure to CO at 100 K are shown in Fig. 3d (except for sample 3.1). The bottom spectra were fitted with a set of contributions from Ce⁴⁺ (doublet peaks 1, 1', 2, and 3) and Ce³⁺ (doublet peaks 4 and 5) cations. For more details about the fitting procedure, we refer to our earlier study.³² The exposure of the samples to CO caused a slight increase of the contributions 4 and 5 associated with a partial conversion of Ce⁴⁺ cations to Ce³⁺. More detailed analysis of the reduction degree of the samples is given below.

CO reaction with Pt–CeO₂: role of segregation

The Pt 4f spectra obtained from samples 1.1 and 1.2 after annealing in CO are plotted in Fig. 4.

Exposure of sample 1.1 to CO at 100 K resulted in a decrease of Pt⁰ and an increase of the Pt* contribution. Typically, CO adsorption in on-top configuration gives rise to a new component in Pt 4f spectra at about 72.0 eV which overlaps with the contribution from Pt* aggregates and cannot be resolved spectroscopically.⁴³ The evolution of the Pt 4f partial contributions is plotted in Fig. 4c as a function of temperature. The data obtained prior to CO exposure are shown in circles. We observe that only contributions from Pt⁰ and Pt* are influenced at 100 K, while the contribution from Pt²⁺ species is not significantly affected. Note that the adsorption of CO on Pt⁰ NPs correlates with the presence of the peak F in the C 1s spectra observed on sample 1.1 (see Fig. 3c). In contrast, we did not observe any major changes in the oxidation state of Pt species for sample 1.2 after the exposure to CO at 100 K. Upon exposure to CO, both samples remained stable below 450 K. At higher temperature, for sample 1.1, we observed the increase of the Pt⁰ contribution at the expense of the Pt²⁺. For sample 1.2, we observed the reduction of the Pt⁴⁺ species yielding Pt⁰ and Pt* at 450 K. However, this behavior results from the limited thermal stability of Pt⁴⁺ species and is not related to the reaction with CO (compare with Fig. 1b). In parallel, the reduction of Pt²⁺ species above 400 K yields Pt⁰ and Pt*. The final oxidation state and composition of samples 1.1 and 1.2 are almost identical. Similar results were obtained by Boronin *et al.*,¹⁶ who observed reduction of Pt⁴⁺ at 423 K (150 °C) simultaneously with a growth of metallic Pt followed by a decrease of the Pt²⁺ contribution at 573 K (300 °C).

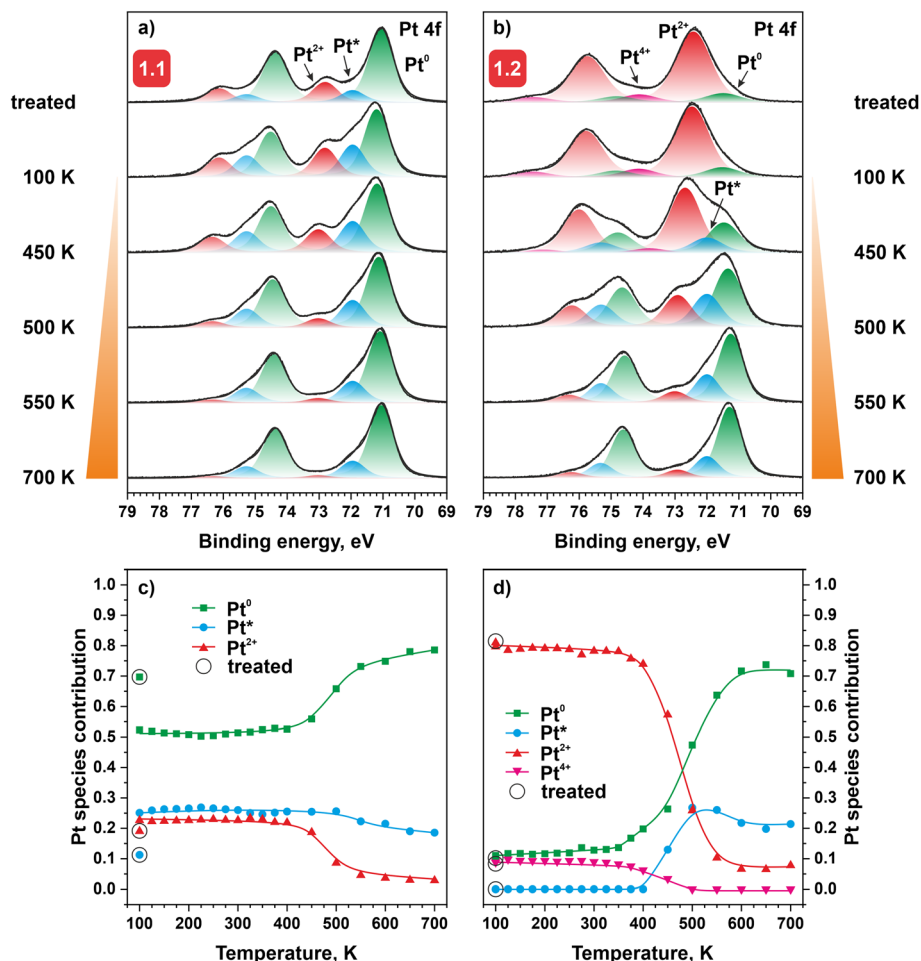


Fig. 4 Pt 4f core level spectra (a and b) and evolution of the integrated relative contributions of the Pt surface species (c and d) as a function of temperature obtained from the treated samples 1.1 (a and c) and 1.2 (b and d) exposed to CO. The Pt 4f spectra were acquired with photon energy of 180 eV.

CO reaction with Pt–CeO₂: role of Pt loading in the absence of Pt segregation

The Pt 4f spectra from samples 2.1 and 3.1 after exposure to CO at different temperatures are shown in Fig. 5. Below 400 K, CO exposure does not influence the oxidation state of the Pt²⁺ species on both samples. However, we observed a gradual shift of the binding energies of the Pt²⁺ species from 72.5 eV to 72.9 eV and from 72.7 eV to 72.9 eV in samples 2.1 and 3.1, respectively. These shifts are caused by the desorption of water, which condensed on the surfaces of both samples. Above 400 K, a Pt* contribution emerges at 450 K on sample 2.1 and grows at the expense of Pt²⁺ species. Above 500 K, the Pt* contribution is accompanied by the Pt⁰ contribution. In contrast, sample 3.1 shows superior stability of the Pt²⁺ species up to 500 K. Above 500 K, both Pt* and Pt⁰ contributions emerge on sample 3.1. These results show that lower thickness and Pt loading in the Pt–CeO₂ catalyst leads to minimized segregation and improved stability of the Pt²⁺ species upon exposure to CO. We attribute the increased stability to the lower platinum content which ensures that there is a sufficient density of {100} nano-pocket sites at the

surface for anchoring the Pt²⁺ species. However, based on the evolution of integrated contributions of Pt species, we observed no redox activity below 400 K for samples 2.1 and 3.1.

CO reaction with Pt–CeO₂: role of ultra-small Pt*/PtO_x species

The Pt 4f spectra obtained from samples 2.2 and 3.2 exposed to CO at different temperatures are shown in Fig. 6.

Note that samples 2.2 and 3.2 were prepared by annealing of samples 2.1 and 3.1 in 1.6 mbar O₂ at 550 K. As mentioned above, we assume that oxidation of the samples containing high amounts of Pt* and Pt⁰ yields a fraction of less stable Pt²⁺ species and ultra-small Pt* and/or PtO_x clusters similar to those reported by Wang *et al.*⁴⁴ The amount of less stable Pt²⁺ species and ultra-small Pt*/PtO_x clusters is higher on sample 2.2 than on sample 3.2. Based on the attenuation of Pt*/PtO_x contribution after CO exposure at 100 K, we assume that ultra-small Pt*/PtO_x clusters also serve as adsorption sites for CO. However, the reaction of CO with these sites does not result in significant changes in the oxidation state of Pt species below 400 K. For sample 2.2, the reduction started above ~400 K, yielding ~55%

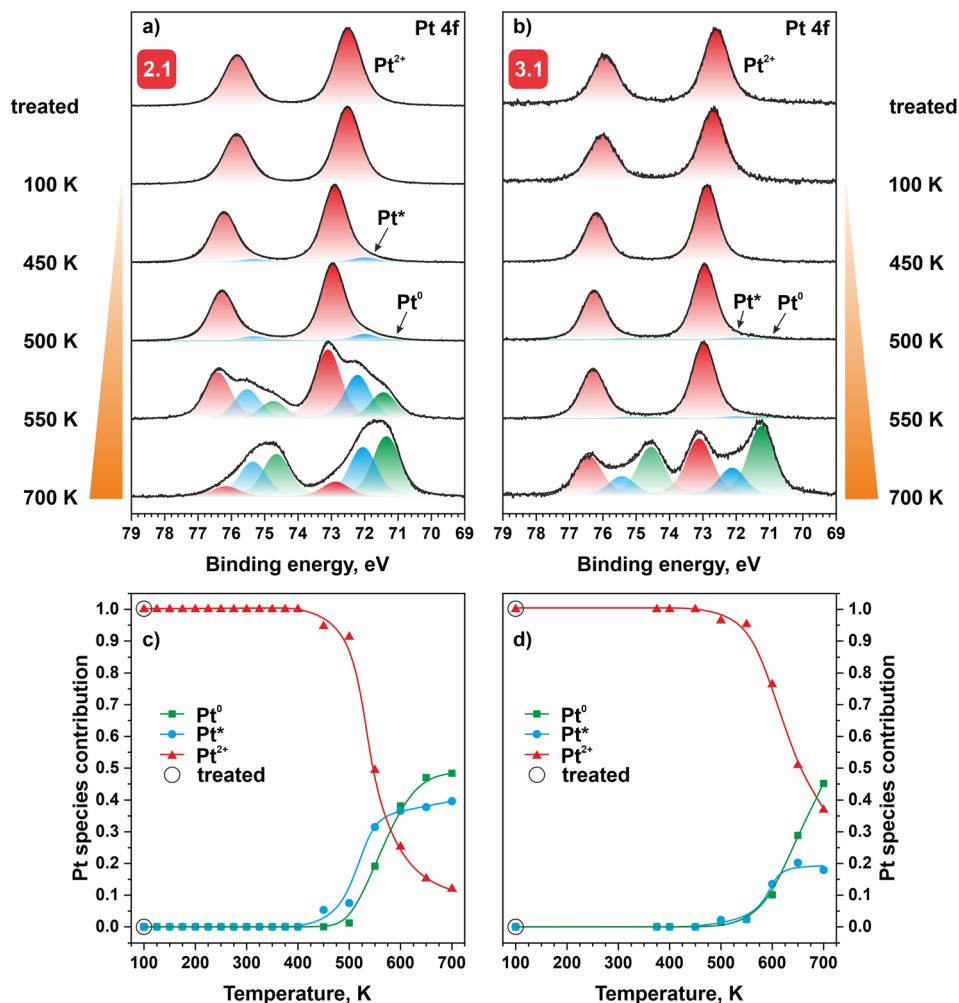


Fig. 5 Pt 4f core level spectra (a and b) and evolution of the integrated relative contributions of the Pt surface species (c and d) as a function of temperature obtained from the treated samples 2.1 (a and c) and 3.1 (b and d) exposed to CO. The Pt 4f spectra were acquired with photon energy of 180 eV.

of Pt⁰ at 700 K. Meanwhile, in sample 3.2, the Pt²⁺ contribution continues to decrease slowly, but even at 700 K the amount of Pt²⁺ species on the surface is still 60% (compared to 15% on sample 2.2). We speculate that for sample 3.2, the density of {100} nano-pocket sites remained sufficient to anchor the majority of Pt²⁺ species.

Involvement of CeO₂ in CO oxidation reaction

The evolution of the Ce³⁺ relative content during exposure to CO is plotted in Fig. 7a as a function of temperature. Prior to CO exposure, the Ce³⁺ relative content in the samples is below 5%, except for sample 1.2 (see circled data in Fig. 7a). The relatively high initial Ce³⁺ relative content in sample 1.2 (~15%) results from contaminations of Pt–CeO₂ film, which could not be removed completely during sample treatment. Upon the first exposure of the samples to CO at 100 K, we observed a minor increase of the Ce³⁺ content due to a slight reduction caused by the formation of carbonates. The onset of more pronounced ceria reduction strongly depends on the nature of Pt species. In

particular, progressive reduction starts at ~200 K for sample 1.1, at ~350 K for sample 1.2, and above 400 K for the other samples. At temperatures above 500 K, we additionally observe partial re-oxidation of ceria.

It is well known that dopants in CeO₂ lead to higher oxygen storage capacity.^{10,16,45,46} A recent study by Boronin *et al.*¹⁶ showed that with increasing Pt loading in CeO₂, the onset of the CO₂ evolution shifts dramatically to lower temperatures. In particular, the authors reported an onset of CO₂ formation in the absence of an external oxygen supply at 270 K (–3 °C) for 20 wt% Pt–CeO₂. For comparison, on pristine CeO₂, CO oxidation starts above ~473 K only (200 °C).¹⁶ The observed low-temperature activity of the 20 wt% Pt–CeO₂ catalyst was explained by the presence of various forms of reactive oxygen on the Pt–CeO₂ catalyst, including some form of PtO_x clusters. Interestingly, in the presence of an external oxygen supply, the 20 wt% Pt–CeO₂ catalyst was found to be active in low-temperature CO oxidation at temperatures as low as 223 K (–50 °C). In a more recent study,¹⁸ the authors proposed a low-temperature mechanism which involves the formation of

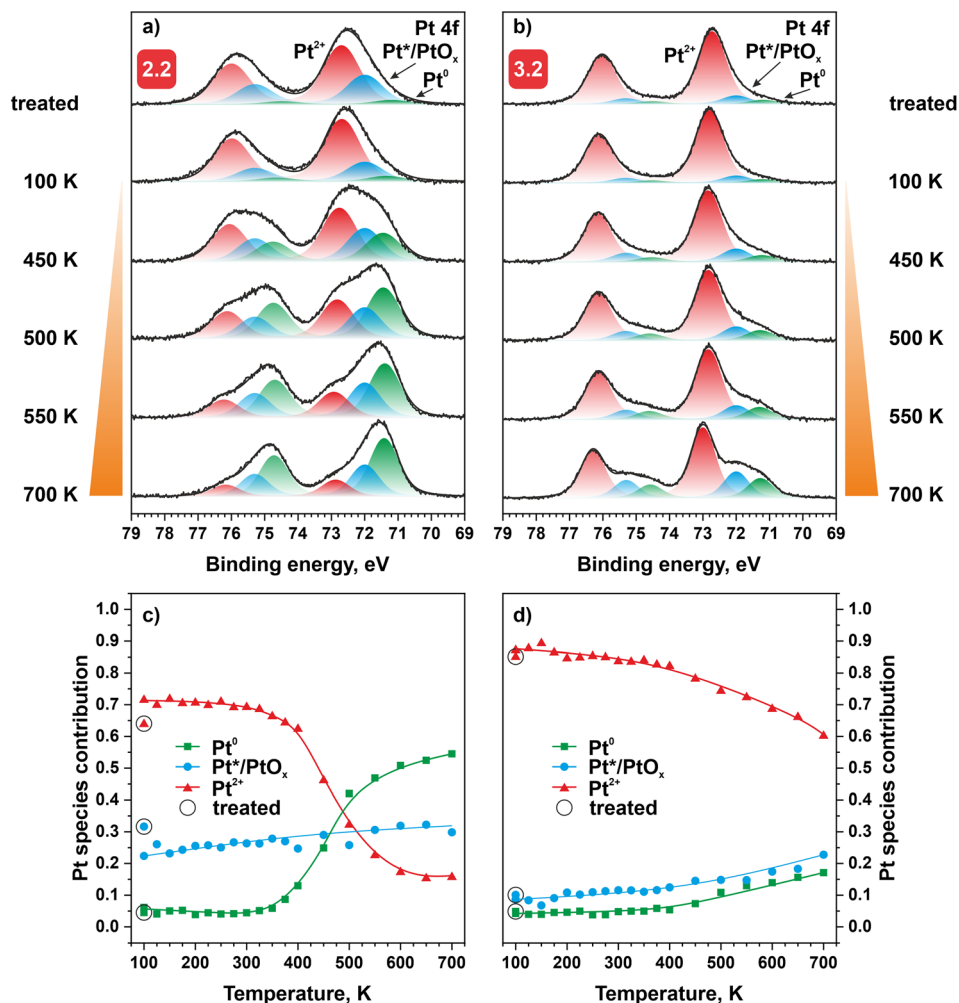


Fig. 6 Pt 4f core level spectra (a and b) and evolution of the integrated relative contributions of the Pt species (c and d) as a function of temperature obtained from the treated samples 2.2 (a and c) and 3.2 (b and d) exposed to CO. The Pt 4f spectra were acquired with photon energy of 180 eV.

weakly bound $(\text{CO})_2\text{O}_2$ complexes on PtO_x clusters. The decomposition of these complexes yields CO_2 without the formation of oxygen vacancies. In this respect, our studies do not indicate any redox interaction between CO and the Pt– CeO_2 catalyst containing PtO_x clusters in the low-temperature region below 400 K.

Also, the low-temperature ceria reduction (<400 K) observed for sample 1.1 cannot be explained in terms of CO interaction with PtO_x clusters. In order to establish the cause of this reduction, we investigated the evolution of the integrated C 1s intensities associated with CO-derived species A, B, and F on sample 1.1 (Fig. 7b). We found a significant increase of the contribution from species B with respect to species A and F between 150 and 275 K. We assume that the corresponding bidentate carbonates form by means of CO spillover from Pt^0 NPs to CeO_2 .⁴⁷ Earlier we reported that bidentate carbonate species on nanostructured Pt-free CeO_2 have low thermal stability. These species decompose above 150 K and do not lead to the formation of oxygen vacancies.²¹ The initial decrease of the C 1s contribution from species B in Fig. 7b is consistent with

this behavior. However, a new more stable bidentate carbonate species B reappears in the spectra above 150 K and resides on the surface up to 275 K. This enhanced stability of the carbonate species B could be related to the increasing degree of reduction of CeO_2 .⁴⁸ We may speculate that these bidentate carbonates will decompose at lower temperatures once oxygen is added to the feed. For instance, Hilaire *et al.*⁴⁹ demonstrated that strongly bonded carbonates on Pd/ CeO_2 are easily decomposed by re-oxidation in O_2 or H_2O .

We note that with the increasing temperature of the catalyst during CO oxidation, additional channels of CO_2 formation will be opened, including the Mars–van Krevelen mechanism^{16–18} and the formation and decomposition of more stable tridentate carbonates A. These channels operate mostly above 400 K and may potentially trigger the reduction of ionic Pt species yielding Pt^* aggregates and metallic Pt^0 NPs. The corresponding effects are coupled with partial re-oxidation of ceria above 500 K (Fig. 7a).

Since metallic Pt^0 NPs are not fully oxidized under realistic CO oxidation conditions,¹⁷ we assume that the redox channel

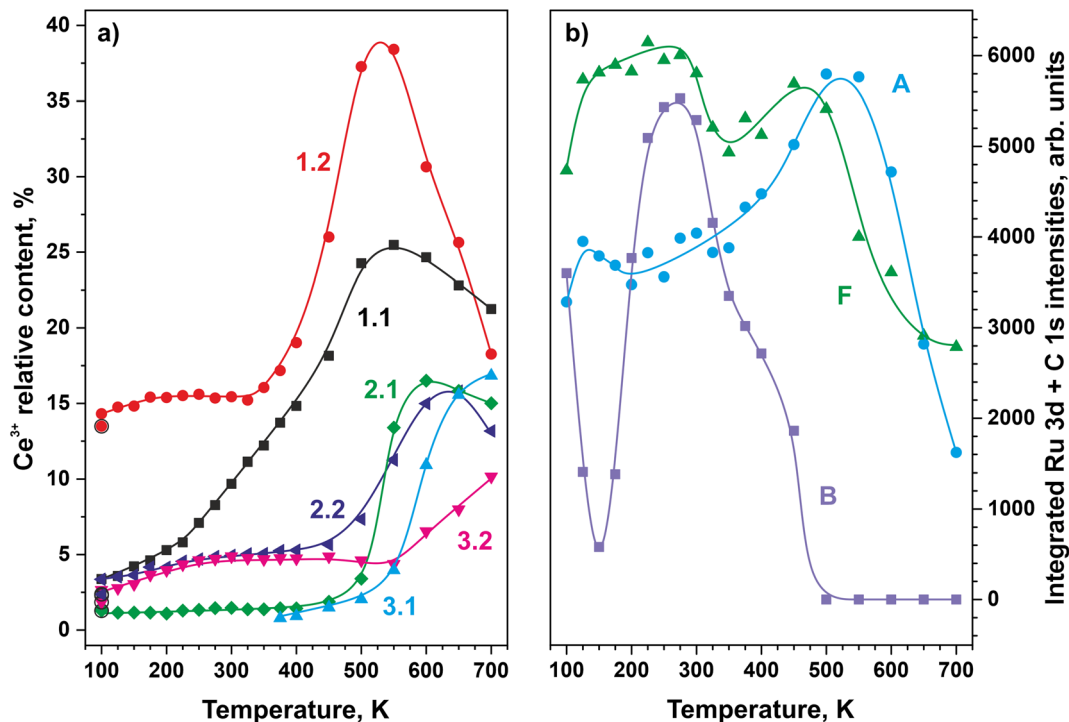


Fig. 7 Ce³⁺ relative content on all studied samples (a) and integrated C 1s intensities on sample 1.1 (b) as a function of temperature after exposure to CO. In (a), the points marked with circles are the relative Ce³⁺ content before exposure to CO. In (b), the species labeled A, B, and F are tridentate carbonates, bidentate carbonates, and CO adsorbed on Pt⁰ NPs, respectively.

associated with CO spillover and formation of bidentate carbonates will play an important role in low-temperature CO oxidation.

Conclusions

We studied the redox capacity of Pt–CeO₂ catalysts containing different forms of platinum species for low-temperature CO oxidation by means of NAP-XPS, SRPES, and RPES. Model Pt–CeO₂ catalysts containing Pt⁰ NPs, ultra-small Pt* aggregates, PtO_x clusters, atomically dispersed Pt²⁺, and Pt⁴⁺ species were prepared by PVD on a well-ordered CeO₂(111) buffer layer on Ru(0001), followed by treatment under reducing and oxidizing conditions. The as-prepared Pt–CeO₂ films differ with respect to the thickness and Pt loading. These parameters have a major influence on the stability of atomically dispersed Pt²⁺ species.

Pt segregation upon annealing of the Pt–CeO₂ films with a nominal thickness of 1.7 nm leads to the formation of Pt⁰ NPs under reducing conditions (annealing in UHV) and Pt⁴⁺ species under strongly oxidizing conditions (annealing at NAP in O₂). The effect of segregation is minimized in the Pt–CeO₂ catalysts with a nominal thickness of 0.4 nm. Accordingly, the formation of Pt⁰ NPs and Pt⁴⁺ species under reducing and oxidizing conditions, respectively, is largely suppressed. By varying the Pt loading, we prepared model Pt–CeO₂ catalysts with different stability of Pt²⁺ species associated with a shortage of anchoring sites — {100} nano-pockets. Additionally, we prepared model Pt–CeO₂ catalysts containing a fraction of Pt²⁺ species in combination with ultra-small Pt*/PtO_x clusters.

Among the studied Pt species, the cationic Pt⁴⁺ sites formed under strongly oxidizing conditions, Pt⁰ NPs, and ultra-small Pt*/PtO_x aggregates serve as adsorption sites for CO at low temperatures. The oxidation states of the Pt species upon annealing in CO do not change below 400 K. Importantly, CO interaction with the Pt–CeO₂ model catalyst containing Pt⁰ NPs triggers the partial reduction of Ce⁴⁺ cations to Ce³⁺ above 200 K. The partial reduction of CeO₂ is associated with bidentate carbonate species formed by means of CO spillover from the Pt⁰ NPs to the support. The formation of CO₂ by decomposition of bidentate carbonates establishes a redox channel for low-temperature CO oxidation on the Pt–CeO₂ catalysts in the presence of Pt⁰ NPs.

Above 400 K, the CO oxidation proceeds for all studied samples according to the Mars–van Krevelen mechanism associated with formation of oxygen vacancies. Above 500 K, subsequent partial re-oxidation of ceria results from the reduction of Pt²⁺ species yielding metallic Pt⁰ NPs and Pt* aggregates.

Our study demonstrates that the nature of the Pt species in the Pt–CeO₂ catalysts controls the mechanisms of low-temperature CO oxidation. The rational design of the corresponding active sites should allow us to maximize the noble metal efficiency of the catalyst.

Author contributions

Alexander Simanenko: formal analysis, investigation, visualization, writing – original draft, writing – review & editing.

Maximilian Kastenmeier: investigation. Lesia Piliai: investigation, writing – review & editing. Yuliia Kosto: investigation, writing – review & editing. Tomáš Skála: investigation, writing – review & editing. Nataliya Tsud: investigation, writing – review & editing. Sascha Mehl: investigation, writing – review & editing. Mykhailo Vorokhta: investigation. Iva Matolínová: funding acquisition, writing – review & editing. Yaroslava Lykhach: conceptualization, investigation, project administration, supervision, writing – review & editing. Jörg Libuda: conceptualization, supervision, writing – review & editing.

Conflicts of interest

There are no conflicts to declare.

Acknowledgements

The authors acknowledge the CERIC-ERIC Consortium for the access to experimental facilities and financial support. The authors acknowledge the support by Czech Ministry of Education, Youth and Sports (project LM2018116) and by Czech Science Foundation (project 20-13573S). The authors thank Dr Kevin Charles Prince for the support and organizing the beamtime. A. S. and Y. L. thank Prof. Konstantin M. Neyman for a fruitful discussion.

References

- 1 Emission Standards, *EU: Cars and Light Trucks*, <https://dieselnet.com/standards/eu/ld.php>, accessed 24 April 2023.
- 2 D. Ciuparu, M. R. Lyubovsky, E. Altman, L. D. Pfefferle and A. Datye, *Catal. Rev.*, 2002, **44**, 593–649.
- 3 V. W. W. Yam, *Nat. Chem.*, 2010, **2**, 790.
- 4 W. Yu, M. D. Porosoff and J. G. Chen, *Chem. Rev.*, 2012, **112**, 5780–5817.
- 5 E. J. Peterson, A. T. DeLaRiva, S. Lin, R. S. Johnson, H. Guo, J. T. Miller, J. Hun Kwak, C. H. F. Peden, B. Kiefer, L. F. Allard, F. H. Ribeiro and A. K. Datye, *Nat. Commun.*, 2014, **5**, 4885.
- 6 A. Bruix, Y. Lykhach, I. Matolínová, A. Neitzel, T. Skála, N. Tsud, M. Vorokhta, V. Stetsovych, K. Ševčíková, J. Mysliveček, R. Fiala, M. Václavů, K. C. Prince, S. Bruyère, V. Potin, F. Illas, V. Matolín, J. Libuda and K. M. Neyman, *Angew. Chem., Int. Ed.*, 2014, **53**, 10525–10530.
- 7 A. Neitzel, V. Johánek, Y. Lykhach, T. Skála, N. Tsud, M. Vorokhta, V. Matolín and J. Libuda, *Appl. Surf. Sci.*, 2016, **387**, 674–681.
- 8 H.-J. Freund, G. Meijer, M. Scheffler, R. Schlögl and M. Wolf, *Angew. Chem., Int. Ed.*, 2011, **50**, 10064–10094.
- 9 J. Ke, W. Zhu, Y. Jiang, R. Si, Y.-J. Wang, S.-C. Li, C. Jin, H. Liu, W.-G. Song, C.-H. Yan and Y.-W. Zhang, *ACS Catal.*, 2015, **5**, 5164–5173.
- 10 K. Ševčíková, T. Kolářová, T. Skála, N. Tsud, M. Václavů, Y. Lykhach, V. Matolín and V. Nehasil, *Appl. Surf. Sci.*, 2015, **332**, 747–755.
- 11 S. Gatla, D. Aubert, G. Agostini, O. Mathon, S. Pascarelli, T. Lunkenbein, M. G. Willinger and H. Kaper, *ACS Catal.*, 2016, **6**, 6151–6155.
- 12 L. Nie, D. Mei, H. Xiong, B. Peng, Z. Ren, X. I. P. Hernandez, A. DeLaRiva, M. Wang, M. H. Engelhard, L. Kovarik, A. K. Datye and Y. Wang, *Science*, 2017, **358**, 1419–1423.
- 13 D. Vasilchenko, T. Asanova, B. Kolesov, A. Tsygankova, A. Stadnichenko, E. Slavinskaya, E. Gerasimov, K. Lomachenko, A. Boronin and S. Korenev, *ChemCatChem*, 2020, **12**, 1413–1428.
- 14 S. Xie, Z. Wang, W. Tan, Y. Zhu, S. Collier, L. Ma, S. N. Ehrlich, P. Xu, Y. Yan, T. Xu, J. Deng and F. Liu, *Environ. Sci. Technol.*, 2021, **55**, 7624–7633.
- 15 L. Liu and A. Corma, *Chem. Rev.*, 2018, **118**, 4981–5079.
- 16 A. I. Boronin, E. M. Slavinskaya, A. Figueroba, A. I. Stadnichenko, T. Y. Kardash, O. A. Stonkus, E. A. Fedorova, V. V. Muravev, V. A. Svetlichnyi, A. Bruix and K. M. Neyman, *Appl. Catal., B*, 2021, **286**, 119931.
- 17 E. M. Slavinskaya, A. I. Stadnichenko, J. E. Quinlivan Domínguez, O. A. Stonkus, M. Vorokhta, B. Šmíd, P. Castro-Latorre, A. Bruix, K. M. Neyman and A. I. Boronin, *J. Catal.*, 2023, **421**, 285–299.
- 18 E. A. Lashina, E. M. Slavinskaya, O. A. Stonkus, A. I. Stadnichenko, A. V. Romanenko and A. I. Boronin, *Chem. Eng. Sci.*, 2023, **267**, 118328.
- 19 A. Neitzel, A. Figueroba, Y. Lykhach, T. Skála, M. Vorokhta, N. Tsud, S. Mehl, K. Ševčíková, K. C. Prince, K. M. Neyman, V. Matolín and J. Libuda, *J. Phys. Chem. C*, 2016, **120**, 9852–9862.
- 20 Y. Lykhach, A. Bruix, S. Fabris, V. Potin, I. Matolínová, V. Matolín, J. Libuda and K. M. Neyman, *Catal. Sci. Technol.*, 2017, **7**, 4315–4345.
- 21 A. Neitzel, Y. Lykhach, T. Skála, N. Tsud, M. Vorokhta, D. Mazur, K. C. Prince, V. Matolín and J. Libuda, *Phys. Chem. Chem. Phys.*, 2014, **16**, 24747–24754.
- 22 Y. Lykhach, A. Figueroba, M. F. Camellone, A. Neitzel, T. Skála, F. R. Negreiros, M. Vorokhta, N. Tsud, K. C. Prince, S. Fabris, K. M. Neyman, V. Matolín and J. Libuda, *Phys. Chem. Chem. Phys.*, 2016, **18**, 7672–7679.
- 23 D. R. Mullins, P. V. Radulovic and S. H. Overbury, *Surf. Sci.*, 1999, **429**, 186–198.
- 24 J.-L. Lu, H.-J. Gao, S. Shaikhutdinov and H.-J. Freund, *Surf. Sci.*, 2006, **600**, 5004–5010.
- 25 N. Nilius, S. M. Kozlov, J.-F. Jerratsch, M. Baron, X. Shao, F. Viñes, S. Shaikhutdinov, K. M. Neyman and H.-J. Freund, *ACS Nano*, 2012, **6**, 1126–1133.
- 26 B. Kaemena, S. D. Senanayake, A. Meyer, J. T. Sadowski, J. Falta and J. I. Flege, *J. Phys. Chem. C*, 2013, **117**, 221–232.
- 27 D. R. Mullins, *Surf. Sci. Rep.*, 2015, **70**, 42–85.
- 28 J. Libra, *KolXPD: Spectroscopy Data Measurement and Processing*, <https://www.kolibrik.net/en/solutions-products/kolxpd>, accessed 24 April 2023.
- 29 V. Matolín, I. Matolínová, L. Sedláček, K. C. Prince and T. Skála, *Nanotechnology*, 2009, **20**, 215706.
- 30 G. N. Vayssilov, Y. Lykhach, A. Migani, T. Staudt, G. P. Petrova, N. Tsud, T. Skála, A. Bruix, F. Illas,

- K. C. Prince, V. Matolin, K. M. Neyman and J. Libuda, *Nat. Mater.*, 2011, **10**, 310–315.
- 31 Y. Lykhach, T. Staudt, M. Vorokhta, T. Skála, V. Johánek, K. C. Prince, V. Matolín and J. Libuda, *J. Catal.*, 2012, **285**, 6–9.
- 32 Y. Lykhach, S. M. Kozlov, T. Skála, A. Tovt, V. Stetsovych, N. Tsud, F. Dvořák, V. Johánek, A. Neitzel, J. Mysliveček, S. Fabris, V. Matolín, K. M. Neyman and J. Libuda, *Nat. Mater.*, 2016, **15**, 284–288.
- 33 A. Figueroba, G. Kovács, A. Bruix and K. M. Neyman, *Catal. Sci. Technol.*, 2016, **6**, 6806–6813.
- 34 F. Dvořák, M. Farnesi Camellone, A. Tovt, N.-D. Tran, F. R. Negreiros, M. Vorokhta, T. Skála, I. Matolínová, J. Mysliveček, V. Matolín and S. Fabris, *Nat. Commun.*, 2016, **7**, 10801.
- 35 K. Kuribayashi and S. Kitamura, *Thin Solid Films*, 2001, **400**, 160–164.
- 36 L. K. Ono, B. Yuan, H. Heinrich and B. R. Cuenya, *J. Phys. Chem. C*, 2010, **114**, 22119–22133.
- 37 D. A. Svintsitskiy, L. S. Kibis, A. I. Stadnichenko, S. V. Koscheev, V. I. Zaikovskii and A. I. Boronin, *ChemPhysChem*, 2015, **16**, 3318–3324.
- 38 B.-H. Mao, E. Crumlin, E. C. Tyo, M. J. Pellin, S. Vajda, Y. Li, S.-D. Wang and Z. Liu, *Catal. Sci. Technol.*, 2016, **6**, 6778–6783.
- 39 F. Pilger, A. Testino, A. Carino, C. Proff, A. Kambolis, A. Cervellino and C. Ludwig, *ACS Catal.*, 2016, **6**, 3688–3699.
- 40 O. Höfert, C. Gleichweit, H. P. Steinrück and C. Papp, *Rev. Sci. Instrum.*, 2013, **84**(9), 093103.
- 41 I. Matolínová, V. Johánek, J. Mysliveček, K. C. Prince, T. Skála, M. Škoda, N. Tsud, M. Vorokhta and V. Matolín, *Surf. Interface Anal.*, 2011, **43**, 1325–1331.
- 42 O. Pozdnyakova, D. Teschner, A. Wootsch, J. Krohnert, B. Steinhauer, H. Sauer, L. Toth, F. Jentoft, A. Knopgericke and Z. Paal, *J. Catal.*, 2006, **237**, 1–16.
- 43 R. Toyoshima, M. Yoshida, Y. Monya, K. Suzuki, K. Amemiya, K. Mase, B. S. Mun and H. Kondoh, *Phys. Chem. Chem. Phys.*, 2014, **16**, 23564–23567.
- 44 H. Wang, J.-X. Liu, L. F. Allard, S. Lee, J. Liu, H. Li, J. Wang, J. Wang, S. H. Oh, W. Li, M. Flytzani-Stephanopoulos, M. Shen, B. R. Goldsmith and M. Yang, *Nat. Commun.*, 2019, **10**, 3808.
- 45 P. Fornasiero, R. Dimonte, G. R. Rao, J. Kaspar, S. Meriani, A. Trovarelli and M. Graziani, *J. Catal.*, 1995, **151**, 168–177.
- 46 T. Montini, M. Melchionna, M. Monai and P. Fornasiero, *Chem. Rev.*, 2016, **116**, 5987–6041.
- 47 E. Lee, J. Lee, S. Hwang and D. H. Kim, *J. Catal.*, 2023, **417**, 421–431.
- 48 G. N. Vayssilov, M. Mihaylov, P. S. Petkov, K. I. Hadjiivanov and K. M. Neyman, *J. Phys. Chem. C*, 2011, **115**, 23435–23454.
- 49 S. Hilaire, X. Wang, T. Luo, R. J. Gorte and J. Wagner, *Appl. Catal., A*, 2004, **258**, 271–276.